Synthesis of char-based adsorbents from cotton textile waste assisted by iron salts at low pyrolysis temperature for Cr(VI) removal

Zhihua Xu[1] · Siyi Gu[1] · Zhenhua Sun[1] · Daofang Zhang[1] · Yuwei Zhou[1] · Yuquan Gao[1] · Renzhi Qi[1] · Weifang Chen[1]

Abstract

Char-based adsorbents (char-FeCl$_3$, char-FeCl$_2$, and char-FeCit) derived from cotton textile waste (CTW) were synthesized by one-step low-temperature pyrolysis approach with different iron salts. The properties of the samples were conducted by BET, SEM, EDS, XRD, XPS, TEM, and FTIR. The results suggested that the surface areas of char-FeCl$_3$ and char-FeCl$_2$ were higher than those of char-FeCit. The presence of Fe$_2$O$_3$ as well as pyrolysis gas (HCl (g) and H$_2$O (g)) could catalyze the formation of porosity. Meanwhile, FeCl$_3$ showed the strongest catalysis effect to decompose cellulose to produce char. The pyrolysis process analysis was investigated by means of thermogravimetry-DSC. FeCl$_3$ and FeCl$_2$ could accelerate the breakage of cellulose structure whereas FeC$_6$H$_5$O$_7$ was not beneficial to form char at low temperature as the incomplete decomposition of citrate. The adsorption property of Cr(VI) for the chars was evaluated. Adsorption processes were fitted well with the Freundlich model, and char-FeCl$_3$ presented the best adsorptive capacity (70.39 mg/g). Thus, this low-temperature pyrolysis method was economical and technologically simplified as well as efficient adsorption capacity of Cr(VI) removal.

Keywords Cotton textile waste · Char · Iron salts · Low pyrolysis temperature · Cr(VI)

Introduction

Activated carbons have been widely applied as the excellent adsorbents in the water treatment. Traditional activated carbons are produced from coal (Cuhadaroglu and Uygun 2008) and wood (Acharyaa et al. 2009) which are expensive and nonrenewable source. In order to overcome the limitation of exhaustible resources, waste materials have attracted much attention to replace conventional raw materials, such as denim fabric waste (Silva et al. 2018), acrylic textile waste (Nahil and Williams 2010), and polyacrylonitrile (Dong et al. 2015). Particularly, cotton textile waste (CTW) contains cellulose

---

Zhihua Xu and Siyi Gu contributed equally to this work and should be considered as co-first authors.

Responsible editor: Tito Roberto Cadaval Jr

✉ Daofang Zhang
  dfzhang_usst@163.com

✉ Weifang Chen
  chenweifang@tsinghua.org.cn

[1] School of Environment and Architecture, University of Shanghai for Science and Technology, 516 Jungong Rd., Shanghai 200093, People's Republic of China

with high-carbon content as a great potential alternative (Chiu and Ng 2012) and cotton-based adsorbent was used in the adsorption of dyes (Chiu and Ng 2012), heavy metal (Muxel et al. 2011), and pharmaceuticals (Sun et al. 2012) in the water treatment as carbon materials.

Commonly, activated carbon is synthesized by physical and chemical activation methods. Physical treatment consists of carbonization and activation, two steps with an activating gas such as CO$_2$ (Daud and Ali 2004) or steam (González et al. 2009). However, physical treatment requires relatively high activated temperature between 800 and 1000 °C. In chemical activation method, some chemical agents including H$_3$PO$_4$, KOH, and ZnCl$_2$ are the most representative activators (Angin 2014; Dutta et al. 2011; He et al. 2016). But, traditional chemical activation also has some drawbacks that contain the damage of equipment resulted from acid or alkali corrosion and high toxicity, which even cause the problem of environmental pollution (Luo et al. 2016). Recently, iron salts are viewed as a novel chemical activator owing to inexpensive and lower toxicity than other chemical agents. In particular, FeCl$_3$ is considered as the most studied activator, which not only have its advantages of catalysis and dehydrogenation but also could bring about remarkable developed porosity (Bedia et al. 2018). Beside, FeCl$_2$ as the catalyst could enhance

et al. 2018). Beside, $FeCl_2$ as the catalyst could enhance pyrolysis of raw materials and production of carbon by reported by Wang et al. (2007). However, activated carbon prepared by $Fe(NO_3)_3$ and $Fe_2(SO_4)_3$ exhibits relatively lower porosity than $FeCl_3$ and $FeCl_2$ due to the presence of chloride ions. In addition, organic iron salts like ferric oxalate (FeC_2O_4) and ferric citrate ($FeC_6H_5O_7$) (Fu et al. 2014) showed different activation pathways. Moreover, $FeC_6H_5O_7$ is not harmful to human and is used in photocatalysis research but it is not studied too much as a chemical activator (Wang et al. 2014).

It is widely accepted that activated method required preparation of the adsorbent at relatively high temperatures (> 600 °C). The utilization of low-temperature method has the potential to save energy consumption and be more economical. It was reported that preparation of activated carbon with $ZnCl_2$ at 400 °C shows good surface area and good adsorption to remove Cr(VI) (Rangabhashiyam and Selvaraju 2015a). Kanungo and Mishr (1996) reported that the dehydration of $FeCl_3$ began at around 40 °C, and then decomposition happened at 100 °C, followed by the formation of Fe_2O_3 during the pyrolysis process. Inspired by transition of iron phase in the range of 40 °C to 300 °C, the feasibility of activated carbon prepared by iron salts at low temperature could be studied. In addition, the mechanism of graphite oxide activation treated by KOH has been investigated below 500 °C (Wu et al. 2016) and Fe^{2+} has comparable catalysis during the cellulose pyrolysis process with K^+ (Wang et al. 2007). On the other hand, carbon contains more C–O and C–H functional groups at low temperatures (300~400 °C) which could provide a platform for removal of adsorbate (Shen and Fu 2018). Hence, three kinds of iron salts ($FeCl_3$, $FeCl_2$, and $FeC_6H_5O_7$) were used as the representative activators to prepare cotton textile waste–based carbon materials at low pyrolysis temperature.

Chromium is commonly used in industries such as leather, metal plating, battery, and textile (Duranoglu et al. 2012). Cr(VI) could transmigrate freely into the ecosystem and organism because of its high solubility and high mobility in the form of $HCrO_4^-$ and CrO_4^{2-} (Liang et al. 2019). It has been noted that Cr(VI) does great harm to human health and has even caused cancers (Salnikow and Zhitkovich 2008). Several methods have been investigated for the removal of Cr(VI), such as ion exchange (Lin and Kiang 2003), biological process (Kumar et al. 2008), extraction (Akama and Sali 2002), and adsorption (Zhang et al. 2015b). Compared to other methods, due to higher efficiency, easier application, and lower cost, the adsorption can be considered as a widely used and promising technique (Liu et al. 2012).

In this study, iron salts were employed to produce the chars derived from CTW via the low-temperature pyrolysis method. The characteristics of chars synthesized by inorganic and organic iron salts were studied by Brunauer-Emmett-Teller (BET), XRD, X-ray photoelectron spectroscopy (XPS), scanning electron microscopy (SEM), transmission electron microscopy (TEM), and FTIR. Thermogravimetry (TG)-DSC was used to further analyze the effect of inorganic and citrate iron salts on the formation of the chars. Finally, adsorption experiments of Cr(VI) were conducted to evaluate the adsorption efficiency of the prepared chars.

Materials and methods

Chemical and materials

CTW was collected in Wuxi, Jiangsu Province, China. Ferric chloride hexahydrate ($FeCl_3 \cdot 6H_2O$), ferrous chloride tetrahydrate ($FeCl_2 \cdot 4H_2O$), ferric citrate ($FeC_6H_5O_7$), hydrochloric acid (HCl), nitric acid (HNO_3), sodium hydroxide (NaOH), and potassium dichromate ($K_2Cr_2O_7$) were purchased from Sinopharm Chemical Reagent Co., Shanghai, China. All experiment procedures were performed by using deionized water (Milli-Q Advantage A10, USA).

Preparation

The CTW was firstly rinsed through deionized water to remove impurities and dried at 50 °C overnight. And CTW was cut into the size of 0.5~1 cm and fully impregnated with 25 mL solutions of different iron salts ($FeCl_3$, $FeCl_2$, and $FeC_6H_5O_7$) in a mass ratio of 3:1 (iron salts:CTW) at 60 °C in a drying oven for 24 h, respectively. Then, these dried mixtures were pyrolyzed at 300 °C for 60 min with a heating rate of 10 °C/min under N_2 flow of 100 mL/min in a furnace and the samples were cooled to room temperature. After that, the samples were soaked in 50 mL boiling HCl solution (1.2 mol/L) and washed with deionized water until the pH of elution was close to neutral. Finally, the resulting chars were dried at 80 °C for 12 h and the prepared chars obtained by $FeCl_3$, $FeCl_2$, and $FeC_6H_5O_7$ were denoted as char-$FeCl_3$, char-$FeCl_2$, and char-FeCit, respectively.

Characterization

The surface area and porosity of chars were investigated with nitrogen adsorption/desorption isotherms at 77 K using a surface area analyzer (Autosorb-iQ 2MP; Quantachrome, USA). The surface area was calculated using the BET equation, and the pore size distributions were calculated by density functional theory (DFT). The total pore volume was defined at the relative pressure (P/P_0) of 0.99. The crystal structures of chars were acquired using powder XRD patterns over a wide range of angles from 10 to 90° (D8 ADVANCE; Bruker, Germany). XPS was carried out using a Kratos Axis Ultra spectrometer with a monochromatic X-ray source of Al Kα operation. The surface morphologies of CTW as well as chars were analyzed by a scanning electron microscope (S4800; Hitachi, Japan),

and energy-dispersive spectrometry (EDS) spectrum was obtained by an energy-dispersive spectrometer (EDAX; Genesis, USA). TEM images of chars were performed by a TEM instrument (Tecnai-G2-F20; FEI, USA). The surface functional groups of samples were explored by a FTIR spectrometer (iS10; Nicolet, China) ranging from 4000 to 400 cm^{-1}. The pyrolysis characteristics of CTW and mixtures of CTW with iron salts (CTW + FeCl$_3$, CTW + FeCl$_2$, and CTW + FeCit) were performed using a TG analyzer (STA 8000; PerkinElmer, USA).

Adsorption experiments

To evaluate the effect of initial pH, 0.1 g of char was added into the Cr(VI) solution (50 mL, 150 mg/L) and the pH values were adjusted to 2~12 with HNO$_3$ (0.1 mol/L) and NaOH (0.1 mol/L). The prepared solution was agitated at a speed of 150 rpm at 25 °C for 12 h. After that, the mixture was passed through a 0.45-μm filter and the concentration of filtered liquor was analyzed by a UV–vis spectrophotometer (Jingke/ UV-754, China). The adsorbed capacity of Cr(VI) was calculated using Eq. (1)

$$q_e = (C_0 - C_e) \cdot V/m \tag{1}$$

where C_0 and C_e (mg/L) are the initial and equilibrium concentrations of Cr(VI), respectively; V (L) is the volume of Cr(VI) solution; and m (g) is the weight of adsorbent.

The adsorption kinetics of Cr(VI) onto chars were studied; 0.2 g of char was mixed with Cr(VI) solution (100 mL, 150 mg/L, initial pH of 2.0) in centrifuge tubes and oscillated at 25 °C with 150 rpm. The concentration of Cr(VI) solution was measured at disparate time periods (10 min, 30 min, 60 min, 120 min, 240 min, 480 min, 720 min, and 1440 min).

The adsorption isothermal model of Cr(VI) onto chars was analyzed; 0.1 g of char was introduced into the Cr(VI) solution (50 mL, 80~300 mg/L, initial pH at 2.0). After 12 h of oscillation at different temperatures (15 °C, 25 °C, and 35 °C), the concentration of Cr(VI) solution was measured.

Results and discussion

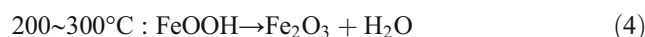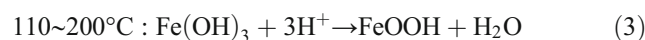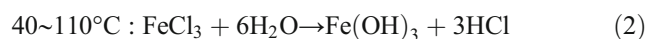### The N$_2$ adsorption/desorption isotherms

The N$_2$ adsorption/desorption isotherms and pore distributions of the chars are depicted in Fig. 1. As shown in Fig. 1a, according to the IUPAC classification, the N$_2$ adsorption/desorption isotherms of both char-FeCl$_3$ and char-FeCl$_2$ exhibited type II with H$_3$ hysteresis loops illustrating the presence of micropores and a large number of mesopores (Bai et al. 2012). For char-FeCit, the isotherm showed almost a straight line with the lowest adsorption

capacity, leading to the relatively low specific surface area and pore volume. According to Fig. 1b, char-FeCl$_3$ and char-FeCl$_2$ had both a small number of micropores and the medium pores with the main proportion, especially between 8 and 25 nm. The porosity of char-FeCl$_2$ was comparable to that of char-FeCl$_3$ due to their similar catalytic effect (Wang et al. 2008). Meanwhile, the pore volume of char-FeCl$_3$ was distinctly greater than that of char-FeCl$_2$. Besides, char-FeCit displayed the lowest porosity which almost had no micropores and mesopores. It could be assumed that the great different properties in three samples were related to disparate thermolysis of inorganic iron salts and iron citrate which have an effect on the CTW (Rudnev et al. 2018).

Furthermore, char-FeCl$_3$ presented the maximum surface area (78 m^2/g) and the largest total pore volume (0.315 m^3/g) among the three samples. The obtained surface areas were comparable to the biochars reported by Hanoğlu et al. (2019) (26.4 m^2/g) from textile fibers. Char-FeCl$_3$ exhibited the multifarious porosity because some iron species might form to develop a pore structure during the pyrolysis process (Oliveira et al. 2009). The BET surface area and total pore volume of char-FeCl$_2$ were 43 m^2/g and 0.119 m^3/g, respectively, indicating that the addition of FeCl$_2$ could also strengthen the generation of pores during the pyrolysis process of CTW. Besides, the yield of char-FeCl$_2$ (48.6%) was higher than that of char-FeCl$_3$ (43.9%). However, char-FeCit displayed the lowest BET (13 m^2/g) and the lowest V_{tot} (0.033 m^3/g).

XRD and XPS

To understand the effect of iron phase evolution on the pyrolysis process, Fig. 2 illustrates the XRD patterns of chars before acid washing. The diffraction pattern of char-FeCl$_3$ was found to be similar to that of char-FeCl$_2$. The patterns of char-FeCl$_3$ and char-FeCl$_2$ showed the peaks at 2θ of 15.7°, 20.5°, 37.7°, 38.8°, 42.2°, 43.4°, 51.8°, 57.8°, and 67.5° were assigned to FeCl$_2\cdot$2H$_2$O; the peaks at 2θ of 32.4° and 33.6° were attributed to the Fe$_2$O$_3$ particles; and the peaks at 2θ of 31.2° were ascribed to FeOOH (Liu et al. 2014). These results suggested that the char might occur in the following reactions ((2)–(4)) (Cazetta et al. 2016):

$$40\text{~}110°C : FeCl_3 + 6H_2O \rightarrow Fe(OH)_3 + 3HCl \tag{2}$$

$$110\text{~}200°C : Fe(OH)_3 + 3H^+ \rightarrow FeOOH + H_2O \tag{3}$$

$$200\text{~}300°C : FeOOH \rightarrow Fe_2O_3 + H_2O \tag{4}$$

The reactions showed that Fe(OH)$_3$ was caused by the hydrolysis of FeCl$_3$, and then converted to FeOOH at the pyrolysis temperature around 100 °C. Next, Fe$_2$O$_3$ was produced from FeOOH when the char was heated to 200 °C. It was
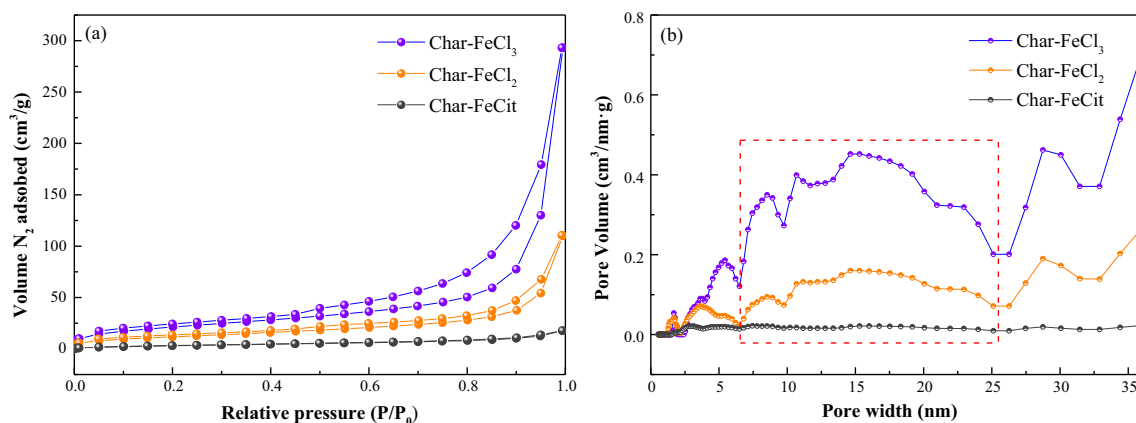
Fig. 1 **a** N_2 adsorption/desorption isotherms of the chars. **b** Pore distributions of the chars

proved that iron compounds had loaded on the interior pore structure of char-FeCl$_3$ and catalyzed to form char at a low temperature of 300 °C. Meanwhile, the reduction of FeCl$_3$· 6H$_2$O to FeCl$_2$·2H$_2$O together with HCl gas was generated to catalyze pore structure (Nicolas Louvain et al. 2013; Oliveira et al. 2009).

Furthermore, it was observed in char-FeCl$_2$ that the peak of FeCl$_2$·2H$_2$O was caused by dehydration of FeCl$_2$·4H$_2$O. In addition, dehydrochlorination of FeCl$_2$·4H$_2$O was transformed to FeOOH and further formed into Fe$_2$O$_3$ species. The observation established that the diffraction intensity of char-FeCl$_2$ was stronger than that of char-FeCl$_3$, which probably was attributed to the better impregnation of FeCl$_2$ (Ohmukai et al. 2008), whereas the pore volume of char-FeCl$_3$ was better than that of char-FeCl$_2$ in Fig. 1b, which is mainly due to the stronger catalysis from Fe^{3+} (Liu et al. 2009).

In contrast, the pattern of char-FeCit demonstrated the peaks at 2θ of 29.5° and 43.2° were attributed to Fe$_3$O$_4$; the peaks at 2θ of 30.0° and 60.5° were assigned to FeOOH; and the peaks at 2θ of 40.0° and 57.8° were ascribed to Fe$_2$O$_3$. The results implied that the decomposition of FeC$_6$H$_5$O$_7$ led to the
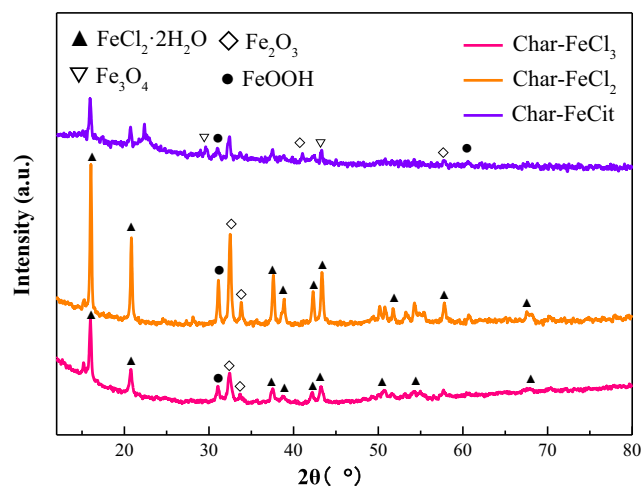
formation of FeOOH and further decomposition and conversion into Fe$_3$O$_4$ species. The converted Fe$_3$O$_4$ played an activated role which facilitated the further formation of pore (Zhang et al. 2016).

XPS survey was performed that aimed at the surface of chars before pickling as shown in Fig. 3a–c. For char-FeCl$_3$ and char-FeCl$_2$, two samples had similar characteristic peaks. The peaks at the binding energy of 710.97 eV and 724.07 eV were ascribed to Fe(III) $2p_{3/2}$ and Fe(III) $2p_{1/2}$, respectively. And of the two chars, the peak at 715.12 eV was the satellite peak of Fe(III) $2p_{3/2}$. At the same time, Fe(II) $2p_{1/2}$ was observed at the peaks of 729.47 eV which was coincided to FeCl$_2$. Moreover, the peaks at 710.97 eV and 724.07 eV can be corresponding to Fe$_2$O$_3$ (Ohmukai et al. 2008). Additionally, it was estimated that the Fe(III) and Fe(II) area ratio was about 7:1 which corresponded to relative Fe$_2$O$_3$ and FeCl$_2$ contents of char-FeCl$_3$ and char-FeCl$_2$. It was confirmed that Fe$_2$O$_3$ was mainly produced by the decomposition of FeCl$_3$·6H$_2$O or FeCl$_2$·4H$_2$O, then further impacting the pore development of chars. Oppositely, the peak positions of Fe $2p_{3/2}$ and Fe $2p_{1/2}$ are 711.27 eV and 724.57 eV, respectively, which were signed to the Fe$_3$O$_4$ in the char-FeCit (Mills and Sullivan 1983). The composition of iron compounds was further determined by XPS analysis. Herein, it was confirmed that the decomposition of inorganic iron salts could induce the formation of Fe$_2$O$_3$, while the ferric citrate pyrolysis resulted in the existence of Fe$_3$O$_4$.

SEM and TEM

The surface morphology was shown by SEM for the comparison of the chars after acid washing. It could be clearly observed in Fig. 4a that raw CTW gave a smooth and soft surface without any pores in its structure. After pyrolysis, the chars exhibited pore structure, indicating that the low-temperature (300 °C) pyrolysis process could led to the development of porosity of raw materials as shown in Fig. 4b–d.
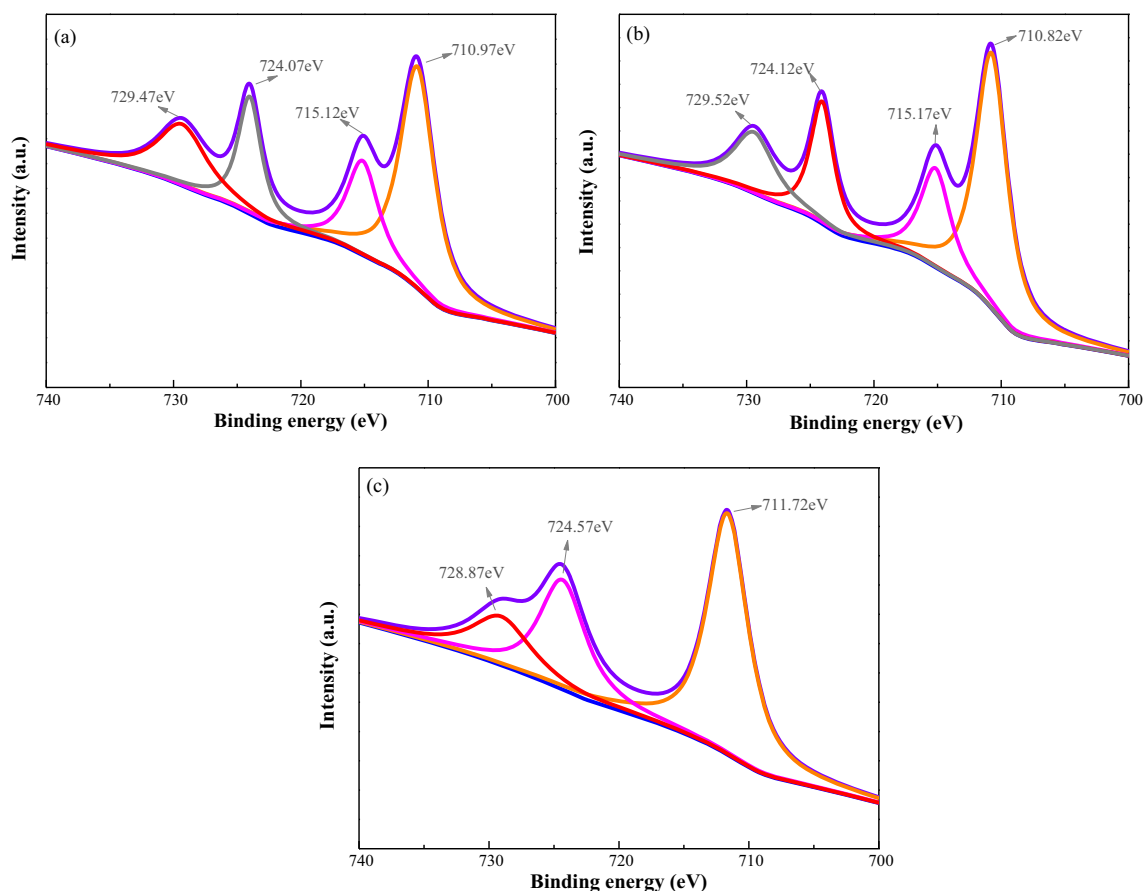

Fig. 2 XRD patterns of the chars

Fig. 3 XPS Fe 2p spectra of **a** char-FeCl$_3$, **b** char-FeCl$_2$, and **c** char-FeCit

a rough and accidented surface, and the char-FeCl$_3$ appeared to have more abundant multiholes than char-FeCl$_2$ which contributed to the increase of the surface area of char-FeCl$_3$. The observed results could be explained that FeCl$_3$ had a stronger effect on the decomposition of cellulose of CTW, facilitating the development of better pore channel (Liu et al. 2009). Besides, Cl$^-$ would combined with chars and cross-linking reactions occurred during the pyrolysis process of CTW with FeCl$_3$ or FeCl$_2$ (Xu et al. 2019). As can be seen in Fig. 4d, char-FeCit showed an entirely different morphology, and the agglomeration phenomenon with the irregular cavity character was observed. The porous structure of char-FeCit was underdeveloped presumably due to the insufficient pyrolysis temperature to decompose citrate and impact the pyrolysis of CTW (Bao et al. 2019).

The SEM-EDS images in Fig. 5a–c display that the C content occupied the dominant location (63.99~79.77%), demonstrating that it was feasible to produce chars at the low-temperature approach. And, a low content of iron existed when iron oxide was loaded on the surface of the three chars after acid washing and iron compounds were covered by chars on the surface's pore structure successfully (Zhang et al. 2015a). The oxygen content mainly came from functional groups of corrupted cellulose as well as formed iron oxide

particles. And, the char-FeCit existed incompletely decomposed citrate which displayed the highest oxygen content.

Figure 6 depicts the TEM image to further characterize the morphologies of the char after acid washing. Some channels of char-FeCl$_3$ and char-FeCl$_2$ had appeared and tended to have an amorphous structure owing to the release of volatiles during the pyrolysis process as shown in Fig. 6a and b. The change of iron phase could increase the porosity during the catalytic pyrolysis process. Additionally, it was noticed that char-FeCl$_3$ possessed more chaotic and compact than char-FeCl$_2$. It was due to that Fe^{3+} had lower accessibility for carbonization of CTW at low temperature (Hamid et al. 2015). However, it was observed in Fig. 6c that few evident bright spots were determined which were assigned to pore structure. The accumulation of iron particles was spread throughout into char-FeCit.

FTIR

Figure 7 presents FTIR spectra of the chars which could analyze the surface functional groups. The bands at around 3428 cm^{-1} of char-FeCl$_3$ and char-FeCl$_2$ and at 3372 cm^{-1} of char-FeCit were ascribed to the O–H stretching vibration of
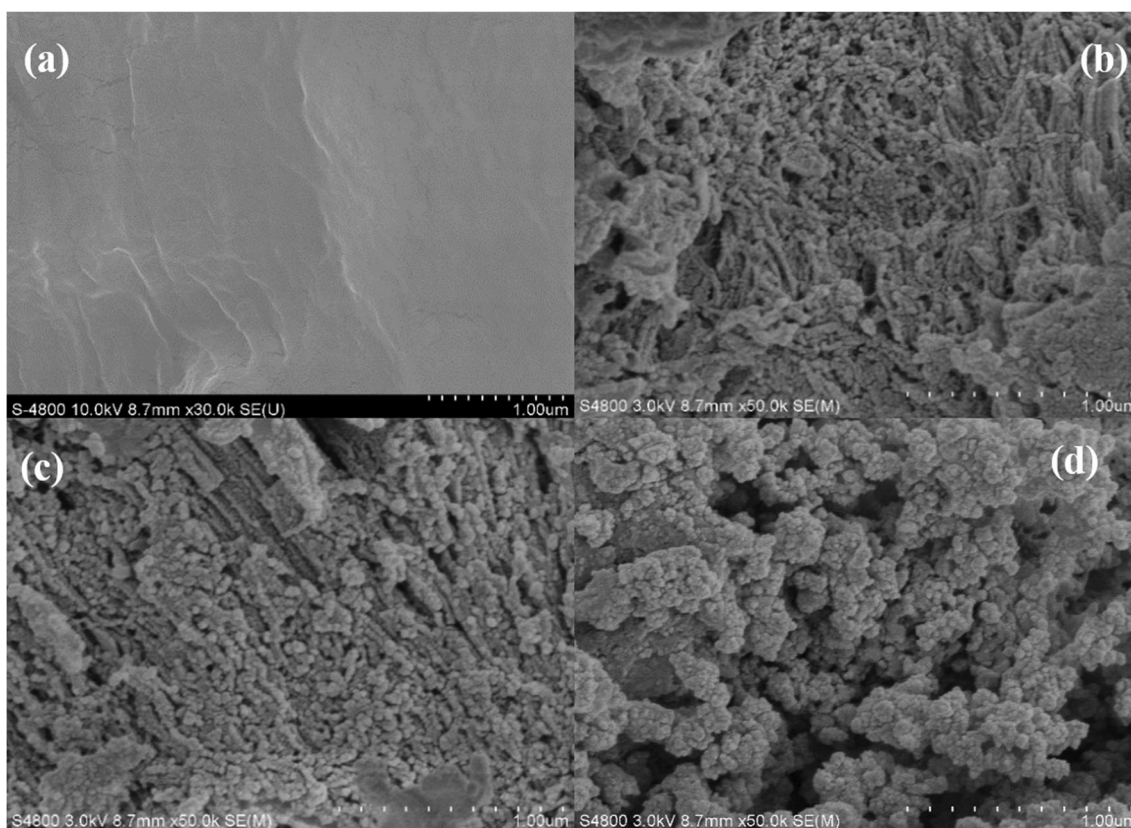
Fig. 4 SEM images of **a** CTW, **b** char-FeCl$_3$, **c** char-FeCl$_2$, and **d** char-FeCit

3428 cm^{-1} of char-FeCl$_3$ and char-FeCl$_2$ and at 3372 cm^{-1} of char-FeCit were ascribed to the O–H stretching vibration of carboxyl and phenol groups. And, a portion of O–H groups was derived from FeOOH and FeCl$_2$·2H$_2$O. Besides, the functional groups of O–H vibration might be involved in the adsorption of metal ions as a participant (Rangabhashiyam and Selvaraju 2015b). The band at between 2920 cm^{-1} and 2900 cm^{-1} was assigned to the C–H stretching vibration of aromatic ring. The band of 1700 cm^{-1} was associated to the C=O vibration of char-FeCl$_3$ and char-FeCl$_2$ in esters or carboxylic groups. Moreover, the band of 1046~1293 cm^{-1} was attributed to the C–O vibration and the C=C vibration of aromatic ring was presented at the band of 1590 cm^{-1} (Nahil and Williams 2010; Sun et al. 2012). The stretching vibration of C–O groups in char-FeCl$_3$ and char-FeCl$_2$ obviously became weaker that corroborated the cellulose from CTW which mostly decomposed and tended to carbonization (Tang et al. 2016). Besides, the band at 670 cm^{-1} was ascribed to the C–Cl groups, indicating that the char-FeCl$_3$ and char-FeCl$_2$ might form a C–Cl bond to grow cross-linking reaction (Lee et al. 2014).

Thermal behavior by TG-DSC analysis

To understand the thermal behavior of the three prepared chars, TG was performed. Figure 8 a–d displays the TG-DSC curve of CTW and mixtures of CTW and iron salts (FeCl$_3$, FeCl$_2$, and FeC$_6$H$_5$O$_7$) under nitrogen to analyze the relation between CTW and iron salts. The TG of CTW (Fig. 8a) could be divided into two stages in the temperature ranges of 0~400 °C. At the primary process below 235 °C, there was the evaporation of moisture mainly with a slight weight loss. The second process with a mass loss of 66.5% was the main pyrolysis process between 235 and 400 °C, attributing to a large number of the collapse of cellulose chains which is accompanied with the release of volatile gases (Mostashari and Mostashari 2008). The DSC enabled to find the endothermic peak at 215 °C which was due to the loss of moisture.

After adding iron salts, it is shown vividly in Fig. 8b–d that the pyrolysis temperature of weight loss is significantly different. For the TG curve of CTW + FeCl$_3$ (Fig. 8b), there were three weight loss steps. The initial weight loss (23.5%) at 0~152 °C was considered for removal of water from CTW, corresponding to an endothermic peak at 97 °C in DSC curve. It was suggested that the addition of FeCl$_3$ promoted the loss of water molecules from CTW. The second weight loss (11.5%) in the range of 152~190 °C occurred in which Fe^{3+} entered the CTW, then strongly fractured the hydrogen bond and glycosidic bond between cellulose (Li et al. 2015), being assigned to the endothermic peak of DSC curve (165 °C). And, the release of H$_2$O molecule was derived from reduction of FeCl$_3$·6H$_2$O to
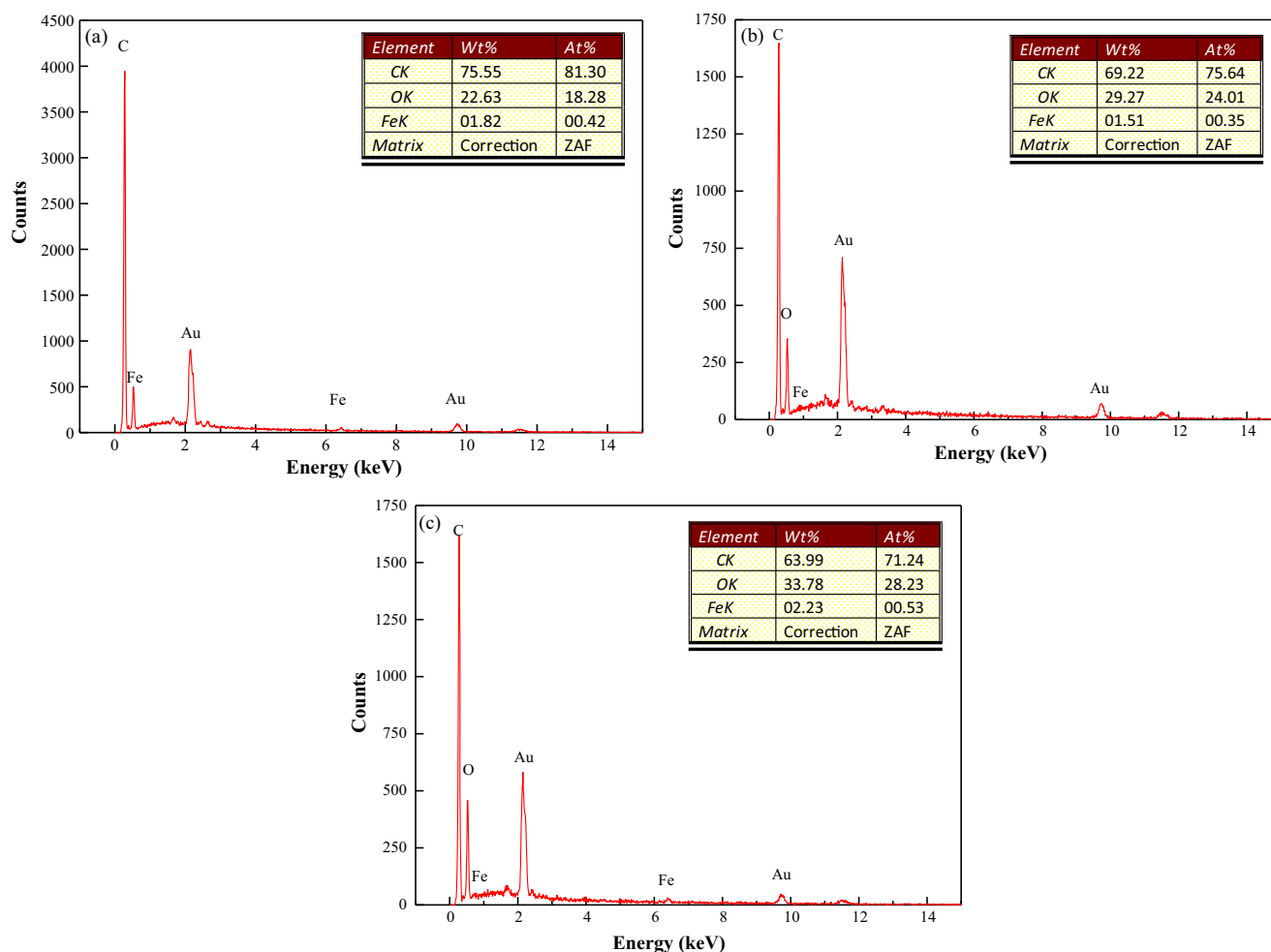
Fig. 5 SEM-EDS spectrum of **a** char-FeCl$_3$, **b** char-FeCl$_2$, and **c** char-FeCit

FeCl$_2 \cdot$2H$_2$O at this temperature stage (Li et al. 2011). The decreasing weight loss was attributed to decomposition of CTW, breaking the structure of the cellulose. And, the volatile matters escaped and left the space in the char matrix. Compared to the TG of CTW, the images provided some interesting finding that the initial pyrolysis temperature was advanced significantly from 235 to 152 °C, which indicated that FeCl$_3$ led to acceleration of the decomposition of cellulose and the pore development was advanced (Rufford et al. 2011). The last stage with the mass loss of 7% at the temperature range of 190 °C and 400 °C had further the decomposition of CTW as well as the production of pyrolysis gas (HCl (g) and H$_2$O (g)). The slope of
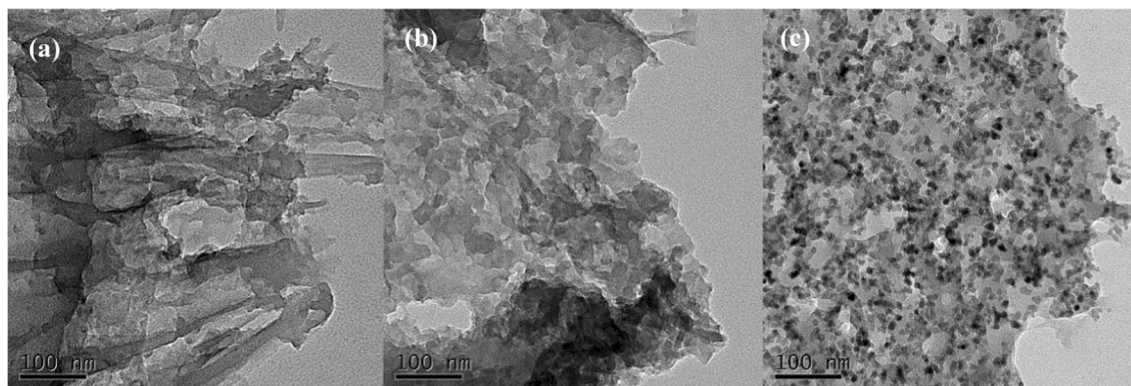

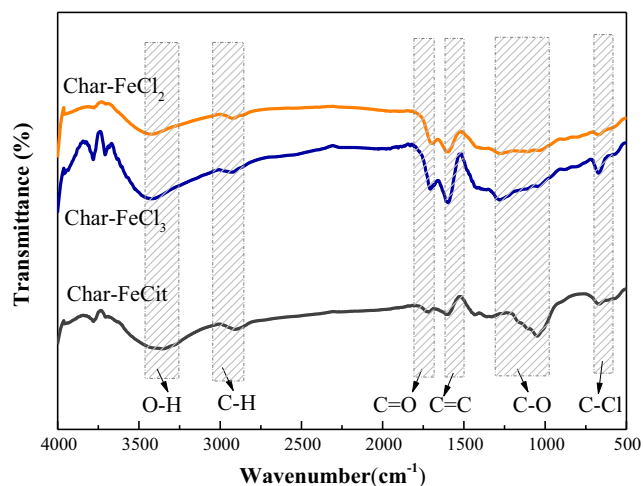**Fig. 6** TEM images of **a** char-FeCl$_3$, **b** char-FeCl$_2$, and **c** char-FeCit

Fig. 7 FTIR spectra of the chars

TG curves became smooth, and the transition of iron phase was caused by the decomposition of $FeCl_2 \cdot 2H_2O$ to Fe_2O_3 (Zhu et al. 2014), which was in accordance with the XRD patterns of char-$FeCl_3$ (Fig. 2). The existence of Fe_2O_3 species was favorable to catalyze pore structure during the catalytic pyrolysis process (Gong et al. 2009). All of these indicated that

doping with $FeCl_3$ as a catalyst accelerated the pyrolysis process of CTW and change the characteristics, creating a pore structure of char-$FeCl_3$.

From Fig. 2c, the TG of CTW + $FeCl_2$ showed three stages. A weight loss of 10% occurred at 0~146 °C which can be attributed to moisture evaporation. The next weight loss of 13.2% was observed between 146 and 204 °C owing to the decomposition of cellulose. It was indicated that $FeCl_2$ could be used as a catalyst and was beneficial to the decomposition reaction during the pyrolysis process (Yuan et al. 2010). Furthermore, the loss of mass was about 7.6% at the temperature of 204~400 °C which was ascribed to transformation of $FeCl_2$ to Fe_2O_3 to facilitate the formation of chars (Nicolas Louvain et al. 2013). In DSC, the initial endothermic peaks at 143 °C belonged to removal of water molecule and the second endothermic peak at 192 °C belonged to decomposition of CTW. The use of ferrous chloride could lead to the disruption of the intermolecular hydrogen bond of cellulose (Yu et al. 2011). When cellulose was decomposed at 146~400 °C, it promoted the release of volatiles and decomposition of CTW because of the addition of $FeCl_2$; in the meantime, the cellulose had trended to collapse to form pore channel. Furthermore, CTW + $FeCl_3$ and CTW + $FeCl_2$ had the same
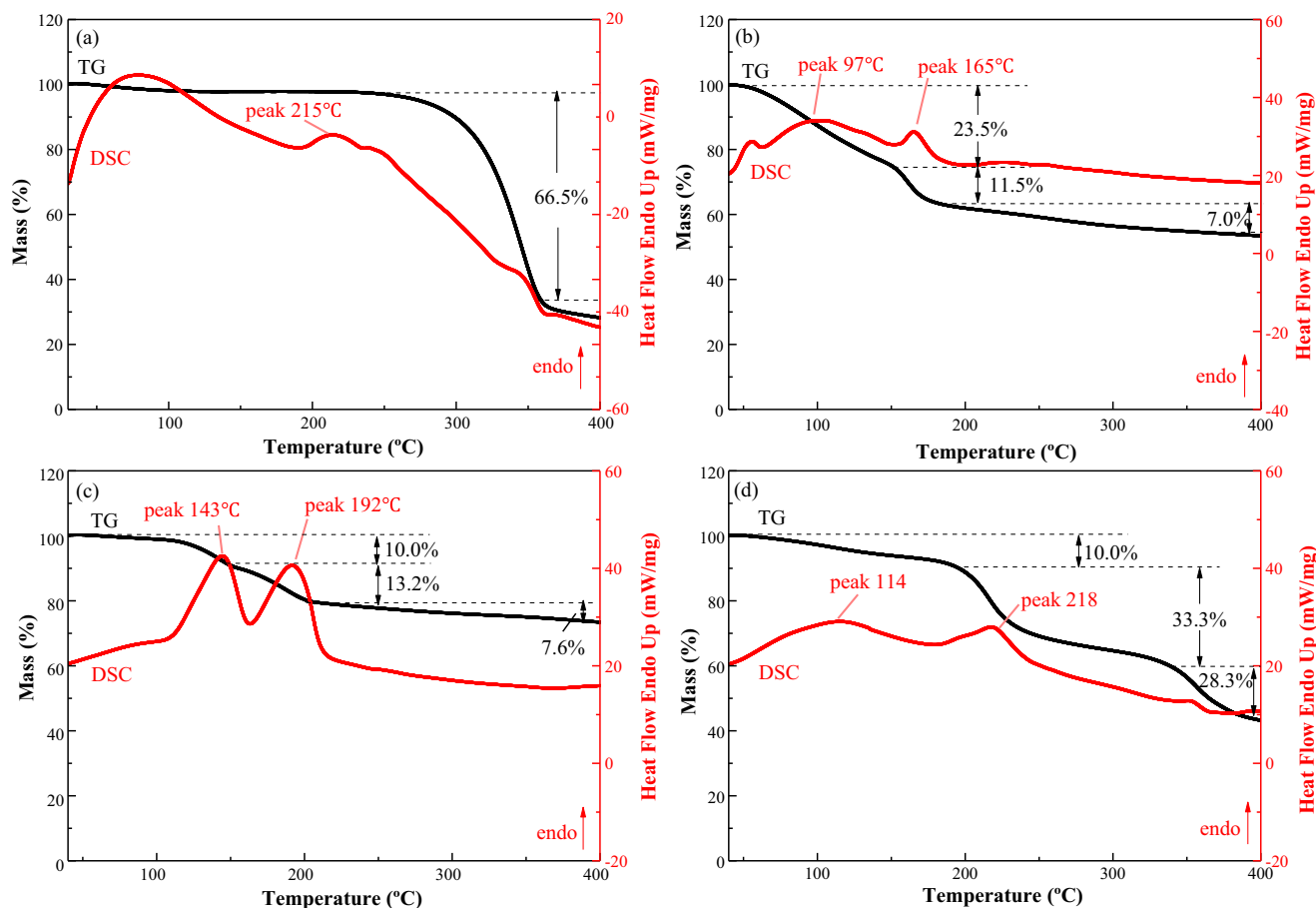

Fig. 8 TG-DSC curves of **a** CTW, **b** CTW + $FeCl_3$, **c** CTW + $FeCl_2$, and **d** CTW + FeCit

trend during the mass loss process. And, the endothermic peak of CTW + FeCl$_2$ became stronger in comparison with that of CTW + FeCl$_3$, which was related to the stronger cleavage degree of cellulose bonds (Hamid et al. 2015). In a word, it was confirmed that FeCl$_2$ played an advantageous role in developing char in the pyrolysis process.

The TG of CTW + FeCit in Fig. 8d had three weight loss steps. In the first step, the weight loss (10%) was ascribed to liberation of absorbed water in the temperature range of 0 °C and 194 °C. In addition, volatilization of crystalline water led to the appearance of endothermic peaks at 114 °C. Compared with the formers, the initial mass loss temperature of CTW + FeCit possibly resulted from the complexation between Fe^{3+} and C$_6$H$_5$O$_7^{3-}$ in aqueous solution (Balachandran 2014), inhibiting the decomposition of ferric citrate. The main weight loss corresponded to the decomposition of FeCit and translation to citraconic and itaconic anhydrides through decarboxylation and dehydration in steps 2 (194~340 °C) and 3 (340~400 °C) (Zhu et al. 2017). The endothermic peak at 218 °C was attributed to the decomposition of CTW. The decomposition of FeCit involved many complex chemical reactions at 300 °C, and the final decomposition product could be corresponded to the organic acids and Fe$_3$O$_4$. The mass loss behavior of CTW with citrate salts appeared to be similar to the results proposed by Zhou et al. (2012) using calcium citrate as the carbon source to prepare porous carbon. Thus, it was suggested that citrate was mainly converted to organic acids before 300 °C and had weak ability to break the structure of cellulose, then decompose CTW at the pyrolysis temperature of 300 °C. The result showed that char-FeCit formed poor pore structure.

Adsorption capacity assessment

The effects of initial pH

The effects of initial pH on the removal of Cr(VI) onto chars are displayed in Fig. 9. The adsorption capacity of Cr(VI) was dependent on initial pH, and the highest removal efficiency was obtained at pH 2. As the pH increased, the predominant ion was HCrO$_4^-$ which gradually converted to CrO$_4^{2-}$ and Cr$_2$O$_7^{2-}$ on the adsorption reaction. In addition, the increased negative charge density with the higher OH$^-$ ions hindered the diffusion of Cr(VI) ions (Liu et al. 2012). Therefore, the efficiency of removal for Cr(VI) declined obviously from pH 4 to 12 due to the electrostatic repulsion between the surface of chars and CrO$_4^{2-}$ (Goswami et al. 2014).

Adsorption kinetics

The kinetic models were analyzed using both the pseudo-first-order and the pseudo-second-order models by the following equations ((5) and (6)):
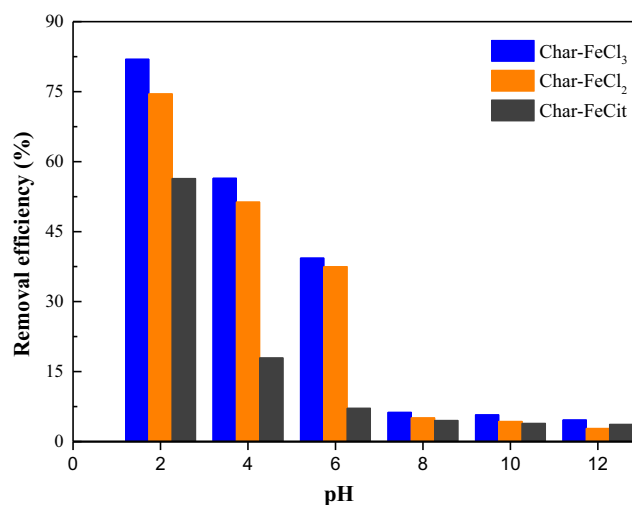

Fig. 9 Effects of initial pH on Cr(VI) adsorption onto chars

Pseudo-first-order model equation

$$q_t = q_e\left(1 - e^{-k_1 t}\right) \tag{5}$$

Pseudo-second-order model equation

$$q_t = \left(k_2 q_e^2 t\right)/\left(1 + k_2 q_e t\right) \tag{6}$$

where q_t and q_e (mg/g) are the adsorption amounts of Cr(VI) at time t and equilibrium, respectively; k_1 (1/min) is the pseudo-first-order rate constant; and k_2 (g/(mg min)) is the pseudo-second-order rate constant.

Figure 10 shows the influence of agitation time of the chars on the adsorption of Cr(VI). With the increasing time, the adsorption efficiency of the chars for Cr(VI) removal went up quickly at first 30 min and then tended to be stable until 720 min, because the adsorption sites of chars were occupied by the adsorbed Cr(VI) (Demiral et al. 2008). As can be seen from Table 1, the adsorption kinetics of Cr(VI) sorption onto
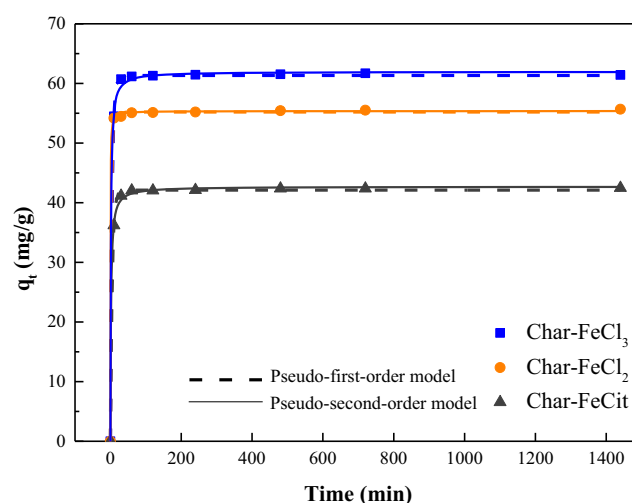

Fig. 10 Effects of time on Cr(VI) adsorption onto chars

Table 1 The parameter of kinetic models for Cr(VI) with different chars

Sample	Pseudo-first-order model			Pseudo-second-order model		
	k_1 (1/min)	q_e (mg/g)	R^2	k_2 ((g/mg)/min)	q_e (mg/g)	R^2
Char-FeCl$_3$	0.2181	61.33	0.99	0.0128	61.96	0.99
Char-FeCl$_2$	0.3980	55.21	0.99	0.0717	55.37	0.99
Char-FeCit	0.1955	42.12	0.99	0.0141	42.69	0.99

chars were both well fitted with pseudo-first-order and pseudo-second-order models, suggesting that chemisorption and physisorption played important roles in the Cr(VI) removal (Liang et al. 2019). The adsorption capacity of three chars ranked from high to low as char-FeCl$_3$ > char-FeCl$_2$ > char-FeCit. On the one hand, the Cr(VI) removal was subjected to oxidation–reduction reaction with the functional groups like O–H and C–O to reduce Cr(VI) and oxidize the chars which led to the expected improved removal efficiency of Cr(VI) (Li et al. 2019). On the other hand, the difference of adsorption capacity was related to the specific surface area of the chars (Bedia et al. 2018). The increasing volume of mesopores was supportive to offer channels and active sites for the movement and adsorption of Cr(VI) (Tang et al. 2016). Besides, the SEM (Fig. 4c) of char-FeCit presented that some

cavities might provide a good chance for the Cr(VI) to be adsorbed (Rangabhashiyam and Selvaraju 2015b). This reason gave an explanation for the feasible adsorption capacity from char-FeCit.

Adsorption isotherms

The adsorption isotherms of Cr(VI) onto chars at different initial concentrations were fitted using the Langmuir and Freundlich models.

The nonlinear form of the Langmuir and Freundlich equations can be expressed as (7) and (8)

$$q_e = q_m K_L C_e / (1 + K_L C_e) \tag{7}$$

$$q_e = K_F C_e^{\frac{1}{n}} \tag{8}$$
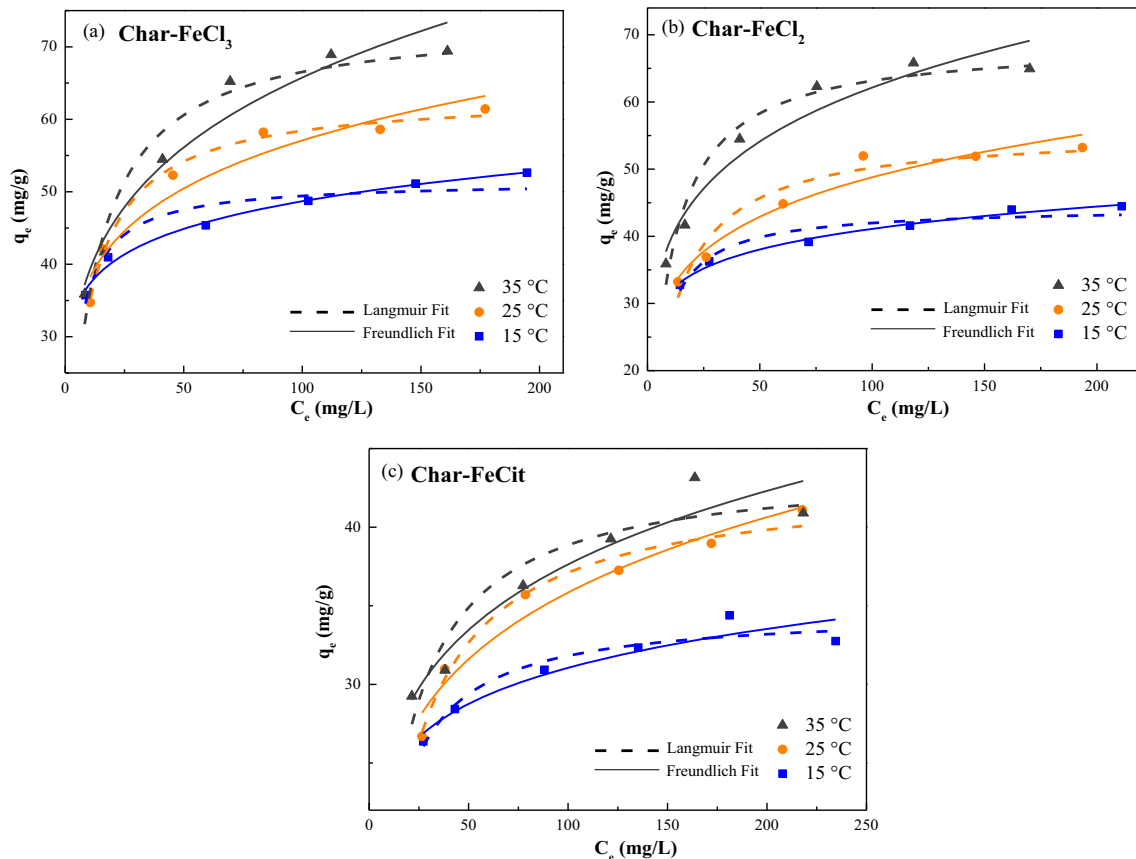

Fig. 11 Langmuir and Freundlich adsorption isotherms fitting of Cr(VI) removal. **a** Char-FeCl$_3$. **b** Char-FeCl$_2$. **c** Char-FeCit

Table 2 Langmuir and Freundlich isotherm model parameters for the adsorption of Cr(VI) on chars

Sample	T (°C)	Langmuir			Freundlich		
		q_m (mg/g)	K_L (L/mg)	R^2	K_F (mg/g(L/mg)$^{1/n}$)	n	R^2
Char-FeCl$_3$	15	51.50	0.24	0.90	28.32	8.49	0.95
	25	64.39	0.12	0.97	25.12	5.60	0.97
	35	73.79	0.10	0.95	22.94	4.37	0.99
Char-FeCl$_2$	15	44.34	0.17	0.90	20.55	8.93	0.99
	25	55.69	0.09	0.93	23.81	5.40	0.94
	35	68.87	0.11	0.96	24.76	5.00	0.99
Char-FeCit	15	34.68	0.11	0.92	18.65	9.02	0.93
	25	42.98	0.06	0.96	15.56	5.52	0.98
	35	43.84	0.09	0.88	17.26	5.91	0.91

where q_e (mg/g) is the adsorption amount of Cr(VI), q_m (mg/g) is the maximum adsorption capacity, C_e (mg/L) is the equilibrium concentration, K_L (L/mg) is the Langmuir constant, and K_F (mg/g(L/mg)$^{1/n}$) is the Freundlich constant.

Figure 11 depicts the Cr(VI) adsorption isotherms onto the chars. The adsorption isotherm explained the relationship between Cr(VI) adsorbed and the concentration in the equilibrium solution. The values of relevant parameters are listed in Table 2, and the maximum adsorption capacity was calculated via the Langmuir model. In the adsorption isotherm study, the chars better fitted with the Freundlich model than the Langmuir model according to the correlation coefficient (R^2), indicating that removal of Cr(VI) onto chars was multilayer coverage (Liu et al. 2012). The separation factor of K_L was between 0 and 1, demonstrating that the adsorption of Cr(VI) onto chars prepared by low pyrolysis temperature was favorable. The value of n between 2 and 10 suggested that the chars were effective adsorbents for Cr(VI) removal. With the increasing temperature, molecular motion was stronger, leading to the increased capacity of Cr(VI) removal, which indicated that the process of Cr(VI) removal with chars could be promoted (Duranoglu et al. 2012).

The maximum adsorption capacity of Cr(VI) onto chars was competitive among the previously reported absorbents derived from different waste materials in Table 3. Compared to the other adsorbents prepared by the relatively high pyrolysis temperature (> 400 °C), the maximum adsorptive capacity of the chars in this study at low-temperature pyrolysis conditions (300 °C) was better. Considering low-energy consumption and environmental friendly method, char-FeCl$_3$, char-FeCl$_2$, and char-FeCit were considered as the feasible and efficient adsorbents for Cr(VI) removal.

Conclusion

Different iron salts served as activating agents to prepare the cotton textile waste–based char adsorbent at the low pyrolysis temperature of 300 °C. It was demonstrated that FeCl$_3$ and FeCl$_2$ had similar characteristics on the breakage of the cellulose and the formation of iron oxides to develop pores during the pyrolysis process. Moreover, the C–Cl bond structure was beneficial to form chars. The best surface area had been produced from char-FeCl$_3$ owing to the highest catalysis effect at low pyrolysis temperature. FeC$_6$H$_5$O$_7$ could promote the decomposition of CTW, but char-FeCit showed unnoticeable porous structures because of the complexation between Fe^{3+} and C$_6$H$_5$O$_7^{3-}$ and inefficient decomposition of citrate. The

Table 3 Comparison of maximum adsorption capacity of Cr(VI) for various adsorbents

Sorbent	Pyrolysis temperature (°C)	q_m (mg/g)	Reference
Bamboo bark–based activated carbon	900	19.53	(Zhang et al. 2015b)
Modified oxidized palm tree branches	–	41.70	(Shouman et al. 2013)
Apple peel–activated carbon	619	36.01	(Enniya et al. 2018)
Matured tea leaf–activated carbon	450	30.08	(Tang et al. 2016)
Corn cob biochar	500	34.48	(Goswami et al. 2014)
Char-FeCl$_3$	300	73.79	This study
Char-FeCl$_2$	300	68.87	This study
Char-FeCit	300	43.84	This study

adsorption behavior of the chars was mostly completed in a short time, which was conformed to pseudo-first-order and pseudo-second-order models while chemisorption and physisorption occurred in the adsorption process. The adsorption equilibrium data followed the Freundlich isotherm model. The order of the adsorption efficiency in relation to BET was char-$FeCl_3$ > char-$FeCl_2$ > char-FeCit. In addition, surface functional groups also provided a platform to improve the adsorption efficiency of Cr(VI). Therefore, it can be concluded that the low-temperature approach to synthesize char-based adsorbents could be employed.

References

Acharyaa J, Sahub JN, Mohantyc CR, Meikap BC (2009) Removal of lead(II) from wastewater by activated carbon developed from tamarind wood by zinc chloride activation. Chem Eng J 149:249–262. https://doi.org/10.1016/j.cej.2008.10.029

Akama Y, Sali A (2002) Extraction mechanism of Cr(VI) on the aqueous two-phase system of tetrabutylammonium bromide and $(NH_4)_2SO_4$ mixture. Talanta 57:681–686

Angin D (2014) Production and characterization of activated carbon from sour cherry stones by zinc chloride. Fuel 115:804–811. https://doi.org/10.1016/j.fuel.2013.04.060

Bai J, Wang Q, Jiao G (2012) Study on the pore structure of oil shale during low-temperature pyrolysis. Energy Procedia 17:1689–1696. https://doi.org/10.1016/j.egypro.2012.02.299

Balachandran M (2014) Bio-processing of indian coals by microorganisms: an investigation. J Environ Res Dev 9:209–215

Bao S et al (2019) In-situ porous nano-Fe_3O_4/C composites derived from citrate precursor as anode materials for lithium-ion batteries. Mater Chem Phys 225:379–383. https://doi.org/10.1016/j.matchemphys.2018.12.072

Bedia J, Belver C, Ponce S, Rodriguez J, Rodriguez JJ (2018) Adsorption of antipyrine by activated carbons from $FeCl_3$-activation of Tara gum. Chem Eng J 333:58–65. https://doi.org/10.1016/j.cej.2017.09.161

Cazetta AL, Pezoti O, Bedin KC, Silva TL, Paesano Junior A, Asefa T, Almeida VC (2016) Magnetic activated carbon derived from biomass waste by concurrent synthesis: efficient adsorbent for toxic dyes. ACS Sustain Chem Eng 4:1058–1068. https://doi.org/10.1021/acssuschemeng.5b01141

Chiu K-L, Ng DHL (2012) Synthesis and characterization of cotton-made activated carbon fiber and its adsorption of methylene blue in water treatment. Biomass Bioenergy 46:102–110. https://doi.org/10.1016/j.biombioe.2012.09.023

Cuhadaroglu D, Uygun OA (2008) Production and characterization of activated carbon from a biuminous coal by chemical activation. Afr J Biotechnol 7:3703–3710. https://doi.org/10.1016/j.protis.2008.04.002

Daud WMAW, Ali WSW (2004) Comparison on pore development of activated carbon produced from palm shell and coconut shell. Bioresour Technol 93:63–69. https://doi.org/10.1016/j.biortech.2003.09.015

Demiral H, Demiral İ, Tümsek F, Karabacakoğlu B (2008) Adsorption of chromium(VI) from aqueous solution by activated carbon derived from olive bagasse and applicability of different adsorption models. Chem Eng J 144:188–196. https://doi.org/10.1016/j.cej.2008.01.020

Dong X, Lu C, Zhou P, Zhang S, Wang L, Li D (2015) Polyacrylonitrile/lignin sulfonate blend fiber for low-cost carbon fiber. RSC Adv 5:42259–42265. https://doi.org/10.1039/c5ra01241d

Duranoglu D, Trochimczukb AW, Bekera U (2012) Kinetics and thermodynamics of hexavalent chromium adsorption onto activated carbon derived from acrylonitrile-divinylbenzene copolymer. Chem Eng J 187:193–202. https://doi.org/10.1016/j.cej.2012.01.120

Dutta S, Bhattacharyya A, Ganguly A, Gupta S, Basu S (2011) Application of response surface methodology for preparation of low-cost adsorbent from citrus fruit peel and for removal of methylene blue. Desalination 275:26–36. https://doi.org/10.1016/j.desal.2011.02.057

Enniya I, Rghioui L, Jourani A (2018) Adsorption of hexavalent chromium in aqueous solution on activated carbon prepared from apple peels. Sustain Chem Pharm 7:9–16. https://doi.org/10.1016/j.scp.2017.11.003

Fu KF et al (2014) Physicochemical and adsorptive properties of activated carbons from Arundo donax Linn utilizing different iron salts as activating agents. J Taiwan Inst Chem Eng 45:3007–3015. https://doi.org/10.1016/j.jtice.2014.08.026

Gong X, Guo Z, Wang Z, Gong X, Guo Z, Wang Z (2009) Variation of char structure during anthracite pyrolysis catalyzed by Fe_2O_3 and its influence on char combustion reactivity. Energy Fuel 23:4547–4552

González JF, Román S, Encinar JM, Martínez G (2009) Pyrolysis of various biomass residues and char utilization for the production of activated carbons. J Anal Appl Pyrolysis 85:134–141. https://doi.org/10.1016/j.jaap.2008.11.035

Goswami M, Borah L, Mahanta D, Phukan P (2014) Equilibrium modeling, kinetic and thermodynamic studies on the adsorption of Cr(VI) using activated carbon derived from matured tea leaves. J Porous Mater 21:1025–1034. https://doi.org/10.1007/s10934-014-9852-1

Hamid SBA, Teh SJ, Lim YS (2015) Catalytic hydrothermal upgrading of α-cellulose using iron salts as a Lewis acid. BioResources 10:5974–5986. https://doi.org/10.15376/biores.10.3.5974-5986

Hanoğlu A, Cay A, Yanık J (2019) Production of biochars from textile fibres through torrefaction and their characterisation. Energy 166:664–673. https://doi.org/10.1016/j.energy.2018.10.123

He J et al (2016) Preparation of highly porous carbon from sustainable α-cellulose for superior removal performance of tetracycline and sulfamethazine from water. RSC Adv 6:28023–28033. https://doi.org/10.1039/c6ra00277c

Kanungo SB, Mishr SK (1996) Thermal dehydration and decomposition of $FeCl_3 \cdot xH_2O$. J Therm Anal 46:1487–1500

Kumar R, Bishnoi NR, Garima, Bishnoi K (2008) Biosorption of chromium(VI) from aqueous solution and electroplating wastewater using fungal biomass. Chem Eng J 135:202–208. https://doi.org/10.1016/j.cej.2007.03.004

Lee SM, Choi WJ, Hwang K, Kim J-H, Lee J-Y (2014) Effect of catalyst concentration and reaction time on one-step synthesized hypercrosslinked polyxylene. Macromol Res 22:481–486. https://doi.org/10.1007/s13233-014-2065-2

Li W-H, Yue Q-Y, Gao B-Y, Wang X-J, Qi Y-F, Zhao Y-Q, Li Y-J (2011) Preparation of sludge-based activated carbon made from paper mill sewage sludge. Desalination 278:179–185. https://doi.org/10.1016/j.desal.2011.05.020

Li J, Zhang X, Zhang M, Xiu H, He H (2015) Ultrasonic enhance acid hydrolysis selectivity of cellulose with HCl-$FeCl_3$ as catalyst. Carbohydr Polym 117:917–922. https://doi.org/10.1016/j.carbpol.2014.10.028

Li B et al (2019) Facile modification of activated carbon with highly dispersed nano-sized α-Fe_2O_3 for enhanced removal of hexavalent chromium from aqueous solutions. Chemosphere 224:220–227. https://doi.org/10.1016/j.chemosphere.2019.02.121

Liang H, Song B, Peng P, Jiao G, Yan X, She D (2019) Preparation of three-dimensional honeycomb carbon materials and their adsorption of Cr(VI). Chem Eng J 367:9–16. https://doi.org/10.1016/j.cej.2019.02.121

Lin SH, Kiang CD (2003) Chromic acid recovery from waste acid solution by an ion exchange. Chem Eng J 92:193–199. https://doi.org/10.1016/S1385-8947(02)00140-7

Liu L, Sun J, Cai C, Wang S, Pei H, Zhang J (2009) Corn stover pretreatment by inorganic salts and its effects on hemicellulose and cellulose degradation. Bioresour Technol 100:5865–5871. https://doi.org/10.1016/j.biortech.2009.06.048

Liu W, Zhang J, Zhang C, Ren L (2012) Preparation and evaluation of activated carbon-based iron-containing adsorbents for enhanced Cr(VI) removal: mechanism study. Chem Eng J 189–190:295–302. https://doi.org/10.1016/j.cej.2012.02.082

Liu WJ, Tian K, He YR, Jiang H, Yu HQ (2014) High-yield harvest of nanofibers/mesoporous carbon composite by pyrolysis of waste biomass and its application for high durability electrochemical energy storage. Environ Sci Technol 48:13951–13959. https://doi.org/10.1021/es504184c

Louvain N et al (2013) One-shot versus stepwise gas–solid synthesis of iron trifluoride: investigation of pure molecular F2 fluorination of chloride precursors. CrystEngComm 15:3664–3671. https://doi.org/10.1039/c3ce27033e

Luo Y, Street J, Steele P, Entsminger E, Guda V (2016) Activated carbon derived from pyrolyzed pinewood char using elevated temperature, KOH, H_3PO_4, and H_2O_2. BioResources 11:10433–10447. https://doi.org/10.15376/biores.11.4.10433-10447

Mills P, Sullivan JL (1983) A study of the core level electrons in iron and its three oxides by means of X-ray photoelectron spectroscopy. J Phys D Appl Phys 16:723–732

Mostashari SM, Mostashari SZ (2008) Combustion pathway of cotton fabrics treated by ammonium sulfate as a flame-retardant studied by TG. J Therm Anal Calorim 91:437–441

Muxel AA, Gimenez SMN, de Souza Almeida FA, da Silva Alfaya RV, da Silva Alfaya AA (2011) Cotton Fiber/ZrO2, a new material for adsorption of Cr(VI) ions in water. Clean: Soil, Air, Water 39:289–295. https://doi.org/10.1002/clen.201000165

Nahil MA, Williams PT (2010) Activated carbons from acrylic textile waste. J Anal Appl Pyrolysis 89:51–59. https://doi.org/10.1016/j.jaap.2010.05.005

Ohmukai Y, Hasegawa I, Fujisawa H, Okuma O, Mae K (2008) Production of an iron-loaded carbonaceous material through pyrolyzing biomass impregnated with FeCl2. Fuel 87:2041–2049. https://doi.org/10.1016/j.fuel.2007.12.013

Oliveira LC, Pereira E, Guimaraes IR, Vallone A, Pereira M, Mesquita JP, Sapag K (2009) Preparation of activated carbons from coffee husks utilizing FeCl3 and ZnCl2 as activating agents. J Hazard Mater 165:87–94. https://doi.org/10.1016/j.jhazmat.2008.09.064

Rangabhashiyam S, Selvaraju N (2015a) Adsorptive remediation of hexavalent chromiumfromsynthetic wastewater by a natural and ZnCl2 activated Sterculia guttata shell. J Mol Liq 207:39–49. https://doi.org/10.1016/j.molliq.2015.03.018

Rangabhashiyam S, Selvaraju N (2015b) Efficacy of unmodified and chemically modified Swietenia mahagoni shells for the removal of hexavalent chromium from simulated wastewater. J Mol Liq 209:487–497. https://doi.org/10.1016/j.molliq.2015.06.033

Rudnev VS, Morozova VP, Lukiyanchuk IV, Tkachenko IA, Adigamova MV, Nedozorov PM (2018) The effect of iron precursors in an electrolyte on the formation, composition, and magnetic properties of oxide coatings on titanium. Prot Met Phys Chem 53:1005–1014. https://doi.org/10.1134/s2070205117060193

Rufford TE, Hulicova-Jurcakova D, Zhu Z, Lu GQ (2011) A comparative study of chemical treatment by FeCl3, MgCl2, and ZnCl2 on microstructure, surface chemistry, and double-layercapacitance of carbons

from waste biomass. J Mater Res 25:1451–1459. https://doi.org/10.1557/JMR.2010.0186s

Salnikow K, Zhitkovich A (2008) Genetic and epigenetic mechanisms in metal carcinogenesis and cocarcinogenesis: nickel, arsenic, and chromium. Chem Res Toxicol 21:28–44. https://doi.org/10.1021/tx700198a

Shen Y, Fu Y (2018) KOH-activated rice husk char via CO2 pyrolysis for phenol adsorption. Mater Today Energy 9:397–406. https://doi.org/10.1016/j.mtener.2018.07.005

Shouman MA, Fathy NA, Khedr SA, Attia AA (2013) Comparative biosorption studies of hexavalent chromium ion onto raw and modified palm branches. Adv Phys Che 2013:1–9. https://doi.org/10.1155/2013/159712

Silva TL, Cazetta AL, PSC S, Zhang T, Asefa T, Almeida VC (2018) Mesoporous activated carbon fibers synthesized from denim fabric waste: efficient adsorbents for removal of textile dye from aqueous solutions. J Clean Prod 171:482–490. https://doi.org/10.1016/j.jclepro.2017.10.034

Sun Y, Yue Q, Gao B, Li Q, Huang L, Yao F, Xu X (2012) Preparation of activated carbon derived from cotton linter fibers by fused NaOH activation and its application for oxytetracycline (OTC) adsorption. J Colloid Interface Sci 368:521–527. https://doi.org/10.1016/j.jcis.2011.10.067

Tang S, Chen Y, Xie R, Jiang W, Jiang Y (2016) Preparation of activated carbon from corn cob and its adsorption behavior on Cr(VI) removal. Water Sci Technol 73:2654–2661. https://doi.org/10.2166/wst.2016.120

Wang S, Liu Q, Liao Y, Luo Z, Cen K (2007) A study on the mechanism research on cellulose pyrolysis under catalysis of metallic salts. Korean J Chem Eng 24:336–340

Wang M, Ren K, Wang L (2008) Iron-catalyzed ligand-free carbon-selenium (or tellurium) coupling of arylboronic acids with diselenides and ditellurides. Adv Synth Catal 351:1586–1594. https://doi.org/10.1002/adsc.200900095

Wang L, Yao Y, Sun L, Mao Y, Lu W, Huang S, Chen W (2014) Rapid removal of dyes under visible irradiation over activated carbon fibers supported Fe(III)–citrate at neutral pH. Sep Purif Technol 122:449–455. https://doi.org/10.1016/j.seppur.2013.11.029

Wu S, Chen G, Kim NY, Ni K, Zeng W, Zhao Y, Tao Z, Ji H, Lee Z, Zhu Y (2016) Creating pores on graphene platelets by low-temperature KOH activation for enhanced electrochemical performance. Small 12:2376–2384. https://doi.org/10.1002/smll.201503855

Xu Z, Tian D, Sun Z, Zhang D, Zhou Y, Chen W, Deng H (2019) Highly porous activated carbon synthesized by pyrolysis of polyester fabric wastes with different iron salts: pore development and adsorption behavior. Colloids Surf A Physicochem Eng Asp 565:180–187. https://doi.org/10.1016/j.colsurfa.2019.01.007

Yu Q, Zhuang X, Yuan Z, Qi W, Wang Q, Tan X (2011) The effect of metal salts on the decomposition of sweet sorghum bagasse in flow-through liquid hot water. Bioresour Technol 102:3445–3450. https://doi.org/10.1016/j.biortech.2010.10.084

Yuan J, Giordano C, Antonietti M (2010) Ionic liquid monomers and polymers as precursors of highly conductive, mesoporous, graphitic carbon nanostructures. Chem Mater 22:5003–5012. https://doi.org/10.1021/cm1012729

Zhang X, Li YX, Li GY, Hu CW (2015a) Preparation of Fe/activated carbon directly from rice husk pyrolytic carbon and its application in catalytic hydroxylation of phenol. RSC Adv 5:4984–4992. https://doi.org/10.1039/c4ra13248c

Zhang YJ, Ou JL, Duan ZK, Xing ZJ, Wang Y (2015b) Adsorption of Cr(VI) on bamboo bark-based activated carbon in the absence and presence of humic acid. Colloid Surf A 481:108–116. https://doi.org/10.1016/j.colsurfa.2015.04.050

Zhang S et al (2016) The role and mechanism of K_2CO_3 and Fe_3O_4 in the preparation of magnetic peanut shell based activated carbon. Powder

Technol 295:152–160. https://doi.org/10.1016/j.powtec.2016.03.034

Zhou QQ, Chen XY, Wang B (2012) An activation-free protocol for preparing porous carbon from calcium citrate and the capacitive performance. Microporous Mesoporous Mater 158:155–161. https://doi.org/10.1016/j.micromeso.2012.03.031

Zhu X, Liu Y, Luo G, Qian F, Zhang S, Chen J (2014) Facile fabrication of magnetic carbon composites from hydrochar via simultaneous activation and magnetization for triclosan adsorption. Environ Sci Technol 48:5840–5848. https://doi.org/10.1021/es500531c

Zhu J, Xu D, Wang C, Qian W, Guo J, Yan F (2017) Ferric citrate-derived N-doped hierarchical porous carbons for oxygen reduction reaction and electrochemical supercapacitors. Carbon 115:1–10. https://doi.org/10.1016/j.carbon.2016.12.084